Research Article

Wang Feiyan, Zhang Yali, Luo Siling, Chen Zhiqin, Luo Shanshan, Li Wenkui*

Biochar from de-oiled *Chlorella vulgaris* and its adsorption on antibiotics

https://doi.org/10.1515/chem-2023-0178
received November 1, 2023; accepted December 9, 2023

Abstract: High-performance biochar was prepared using de-oiled *Chlorella vulgaris* biomass as the raw material and KOH as the modifying activator. The properties of the biochar as an adsorbent for the removal of tetracycline (TC) and enrofloxacin (ENR) were investigated under different conditions by varying the amount of the *Chlorella vulgaris* de-oiled biomass (DB) input. The surface structure and physicochemical properties of different *Chlorella vulgaris* biomass charcoal (CBC) samples were studied and compared, and the best adsorption performance of the biomass charcoal was obtained when DB = 7. Through orthogonal analysis, it was determined that the optimal adsorption condition of CBC 7 on TC was 0.004 g (pH 3), which resulted in a removal rate of 96.45% and a maximum adsorption capacity of 241.1363 mg g^{-1}, and on ENR was 0.004 g (pH 7), which resulted in a removal rate of 100% and a maximum adsorption capacity of 256.3326 mg g^{-1}. The results of the kinetic fitting show that the adsorption of TC and ENR by CBC 7 was consistent with the pseudo-secondary kinetic equation. The maximum adsorption capacities can reach 299.8974 and 352.6736 mg g^{-1}. Langmuir and Freundlich adsorption isotherm models were used to describe the adsorption equilibrium of TC and ENR by CBC 7. The results show that the adsorption of TC and ENR are in accordance with the Langmuir isotherm.

Keywords: biochar, *Chlorella vulgaris*, tetracycline, enrofloxacin, adsorption

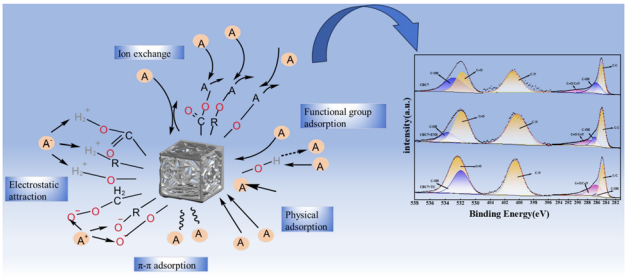

Graphical abstract

1 Introduction

In recent years, rapid urbanization has increased demands for water resources and raised concerns about water pollution. Many low-level but hazardous pollutants, such as antibiotics, endocrine disruptors, and hormone disruptors, known as emerging contaminants (ECs) [1–4], are gradually attracting attention. ECs are a class of chemical pollutants with potential threats to human health and the ecological environment. ECs are often derived from pharmaceuticals, personal care products, endocrine disruptors, antibiotics, disinfection by-products, and other industrial chemicals [5,6]. The common pathways for ECs to enter the environment include wastewater from sewage treatment plants, hospitals, drains, and septic systems, leachate from landfills, and animal wastewater from livestock, poultry processing, and aquaculture [7,8]. Although the levels of these ECs are low, the compounds and transformation products derived from them are ubiquitous in the environment, and those compounds can persist for long periods of time, so there is widespread interest in removing ECs from the aquatic environment.

In order to remove ECs, a number of methods have been developed, which include adsorption, membrane technology [9,10], biological treatment [11], advanced oxidation process, and photocatalytic degradation [12–14]. The adsorption method has the advantages of low cost, a wide range of material sources, and excellent adsorption performance compared to other methods, making it more feasible in actual treatment [15–17]. Commonly used adsorbents include silica gel (SiO_2) [18,19], zeolite [19,20], activated

* **Corresponding author: Li Wenkui**, Jiangxi Key Laboratory of Materials Surface Engineering, Jiangxi Normal University of Science and Technology, Nanchang, 330000, China, e-mail: liwenkui1976@163.com
Wang Feiyan, **Zhang Yali**, **Luo Siling**, **Chen Zhiqin**, **Luo Shanshan:** Jiangxi Key Laboratory of Materials Surface Engineering, Jiangxi Normal University of Science and Technology, Nanchang, 330000, China

carbon (AC), molecular sieve [21], and so on [22]. Among them, AC is widely recognized for its large specific surface area, rich microporous and mesoporous structure, carbon atomic structure that makes it more thermally conductive than silica particles, and stable physical and chemical forms in aqueous solution, but the high cost of manufacturing also affects its inability to be widely used [23–25]. Compared with the expensive AC, biochar has entered the researchers' field of vision due to its advantages of low cost and good performance from a wide range of raw material sources.

Biochar is a porous material produced by the decomposition of biomass feedstocks at high temperatures. Biochar has already demonstrated its excellence in a number of areas. It comes from a wide range of sources and can be any material containing organic matter, including agricultural and forestry waste, wood chips, algae, sludge, fertilizer, and solid organic waste. The surface structure and physicochemical properties of biochar's prepared from different raw materials differ significantly, and these properties are key factors affecting the adsorption performance of biochar. In Kurniawan et al.'s work [26], the production cost of biochar was 30% lower than that of AC. Using industrial lignin as a feedstock, Zhou et al. [27] prepared honeycomb lignin-based biochar by hydrothermal activation, which achieved over 99% removal of norfloxacin in real water within 8 min and maintained at least 98% removal of norfloxacin after 12 adsorption cycles. Among many raw materials, microalgae has been widely studied for its fast growth, rich in oil and protein content, and does not occupy planting areas, etc. Torri et al. [28] used waste algal biomass to convert it into nitrogen-rich biochar, biodiesel, and pyrolysis oil and found that microalgal biochar contained less carbon but more nitrogen, ash, and minerals than biochar produced from lignocellulosic biomass. Biochar with high nitrogen and ash content improved soil quality and productivity. Tso and Chao [29] reported that chlorella biochar was more effective than powdered AC in removing p-nitrophenol from wastewater. Wang et al. [30] produced algal biochar using brown algae as the raw material to remove 97.24% of methyl orange dye. Combined with numerous studies, algal biochar is considered a low-cost adsorbent with special surface chemistry of high adsorption capacity, high porous structure, and high thermal stability [31].

Microalgae are now recognized as a feedstock for third-generation biofuels, showing great potential for biodiesel production [32], and their residue after oil extraction is often referred to as DB [33]. Therefore the production of biochar from DB and its use as an adsorbent for the treatment of pollutants in wastewater is also a potential avenue [34].

In this study, biochar was prepared using de-oiled *Chlorella vulgaris* biomass as the raw materials and KOH as the activator. Its removal mechanism on tetracycline (TC) and enrofloxacin (ENR) was discussed.

2 Materials and methods

2.1 Materials

The microalgae strain, NCU C03, was isolated from the local environment around Nanchang University using the dilution method. BG-11 medium was used for isolation. The algal strain was identified as *Chlorella vulgaris*. The microalgal cells were cultured with a TAP medium.

TC (purity ≥98%) and ENR (purity ≥98%) were from Shanghai Ron Reagent Co. KOH was purchased from Guangxi Xilong Chemical Co. Ethanol, methanol, and other organic solvents were purchased from Tianjin Da Mao Co. The chemicals used in this study were of analytical grade, and the water used in the study was deionized water.

2.2 Biochar preparation

The preparation process of materials is shown in Figure 1. *Chlorella vulgaris* powder was mixed with an ethanol solution and treated with a cell breaker to rupture the cell walls. *Chlorella vulgaris* cells are extracted using the Folch method [35] and centrifuged at 8,000 rpm to obtain a DB slurry. The washed and cleaned DB was frozen at −20°C for 10 h and then dried in a freeze-dryer at −82°C for 48 h.

The dried DB slurry was mixed with KOH and water in a ratio of 1:3:5 and then dried in an oven at 110°C to obtain KOH-activated DB.

DB was carried in a ceramic boat (60 mm × 30 mm × 14 mm) and heat-treated at 750°C in a constant temperature tube furnace (NBD-01200-50IC). The amount of algae biomass varied from 3 to 11 g according to experiment design. After heat treatment, the sample was cooled to room temperature, washed with deionized water to pH 6–7, and then oven-dried. Biochar samples were named CBC 3, CBC 5, CBC 7, CBC 9, and CBC 11, respectively, according to the DB input in the experiment.

2.3 Characterization

The BET-specific surface area, micropore volume, and pore size distribution of the biochar were determined using a specific surface area pore analyzer (Micromeritics Model APSP2460 Specific Surface Area Analyzer, USA). The surface morphology and structure of the biochar were determined using a scanning electron microscope (SEM, Zeiss, Germany). Fourier transform infrared spectrophotometer

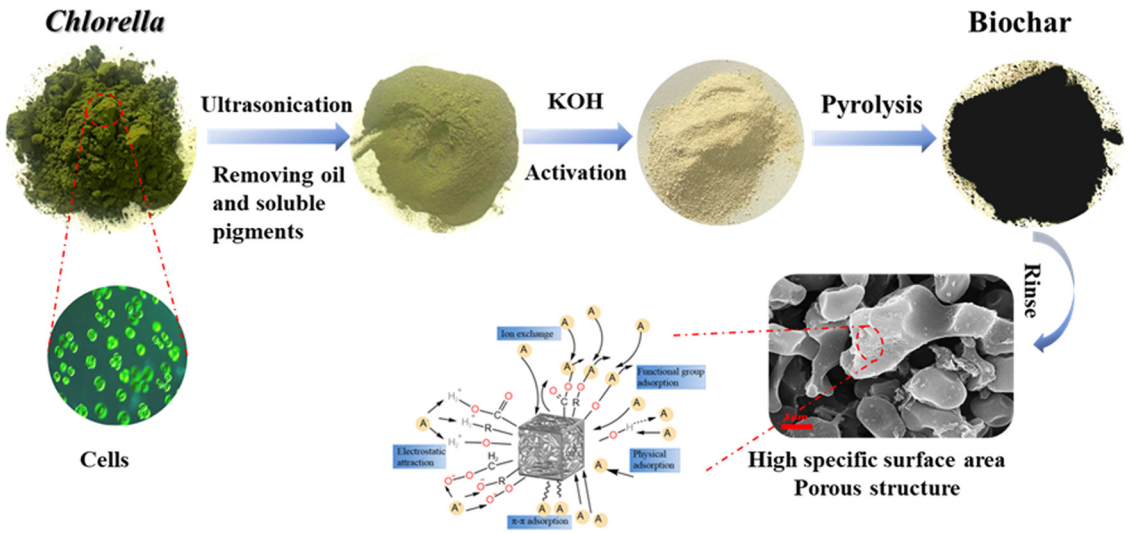

Figure 1: Roadmap of the experiment process.

(FT-IR, Spectrum Two PerkinElmer) was used to study the functional groups of the biochar materials. The chemical composition of the biochar materials was further analyzed using an X-ray photoelectron spectrometer (Thermo Scientific K-Alpha, USA). The structure and crystallinity of the biochar materials were characterized using an X-ray diffractometer (XRD-6100, Shimadzu, Japan).

2.4 Batch experiments

In this study, two parameters, adsorbent input (MCBC) and solution pH, were designed and optimized using the orthogonal design of experiments. These factors were considered at four levels according to the adsorption capacity of CBCx. The L16 orthogonal array was used and the experimental conditions are shown in Table 1. All experiments were conducted three times in parallel to reduce errors in experimental results caused by random events. Statistical analysis is carried out by variance analysis ($p < 0.05$, IBM SPSS Statistics V21).

At room temperature, different masses of CBCx were added into TC and ENR solutions with different pH values for adsorption for 2 h. After the adsorption process, the adsorbent was filtered through a needle filter to obtain the filtrate, and the residual TC and ENR absorbance in the filtrate was determined by UV spectrophotometry at 354 and 265 nm (Table 2).

In the kinetic experiments, 0.004 g of CBCx was added to 10 mL of 100 mg L^{-1} of TC and ENR solutions, respectively. The solutions were stirred continuously at room temperature and sampled at time intervals. The solutions were stirred continuously at room temperature and sampled at time intervals. The absorbance and adsorption kinetics of the value antibiotic (VA) concentration in the solution were measured using a UV spectrophotometer.

Table 1: Controlled factors and their levels

Factors	Symbol	X			
		Level 1	Level 2	Level 3	Level 4
MCBC (g mL^{-1})	X_1	0.002 g	0.004 g	0.006 g	0.008 g
pH	X_2	3	5	7	10

Table 2: Experimental results obtained by orthogonal analysis

No.	Name	M_{CBC} (g mL^{-1})	pH
1	N1	0.0002	3
2	N2	0.0002	5
3	N3	0.0002	7
4	N4	0.0002	10
5	N5	0.0004	3
6	N6	0.0004	5
7	N7	0.0004	7
8	N8	0.0004	10
9	N9	0.0006	3
10	N10	0.0006	5
11	N11	0.0006	7
12	N12	0.0006	10
13	N13	0.0008	3
14	N14	0.0008	5
15	N15	0.0008	7
16	N16	0.0008	10

In order to study the isothermal adsorption experiments of CBCx adsorption on TC and ENR and their thermodynamic properties, 0.004 g of CBCx was added to 10 ml of TC and ENR solutions of different concentrations (100, 105, 110, 115, 120, and 125 mg L^{-1}) at temperature gradients of 298, 308, and 318 K, respectively. The solution was stirred continuously for 120 min at the corresponding temperature gradient. The absorbance of the VA concentration in the solution is measured using a UV spectrophotometer.

2.5 Model fitting

The maximum adsorption capacity and removal rate of CBCx were calculated using the absorbance of residual TC and ENR in the filtrate measured in Section 2.4:

Removal rate H (equation (1)):

$$H = \frac{C_0 - C_e}{C_0} \times 100\%. \tag{1}$$

Adsorption capacity q_e (equation (2)):

$$q_e = \frac{(C_0 - C_e) \times V}{m}, \tag{2}$$

where C_0 and C_e are the initial and final concentrations (mg L^{-1}) of target pollutants TC and ENR, respectively, V is the initial solution volume (L), and m is the mass of the adsorbent (g).

The adsorption kinetic results were fitted using pseudo-first-order [36] (equation (3)), pseudo-second-order [37] (equation (4)), and Elovich [37] (equation (5)) models for adsorption kinetic results.

$$\frac{dq_t}{dt} = k_1(q_e - q_t), \tag{3}$$

$$\frac{dq_t}{q_t} = k_2(q_e - q_t)^2, \tag{4}$$

$$q_t = \frac{1}{\beta}\ln(\alpha\beta) + \frac{1}{\beta}\ln t, \tag{5}$$

where q_t and q_e (mg g^{-1}) are the adsorption amount of adsorbate on the adsorbent surface at time t and adsorption equilibrium, respectively. k_1 (min^{-1}) is the pseudo-first adsorption rate constant, k_2 (g mg min^{-1}) is the pseudo-second adsorption rate constant, α (mg g^{-1} min^{-1}) is the initial adsorption rate constant, and β (g mg^{-1}) is the rate constant related to the surface coverage and chemisorption activation energy.

Isothermal adsorption was determined by fitting the relationship between the adsorption concentration and adsorption capacity at equilibrium using the adsorption isotherm models of Langmuir [38] (equation (6)) and Freundlich [39] (equation (7)).

$$q_e = \frac{q_m k_L C_e}{1 + k_L C_e}, \tag{6}$$

$$q_e = k_F C_e^{1/n}, \tag{7}$$

where C_e (mg L^{-1}) is the residual concentration of the adsorbent in solution at adsorption equilibrium, q_e (mg g^{-1}) is the adsorption amount of the adsorbent on the adsorbent surface at adsorption equilibrium, q_m (mg g^{-1}) is the adsorption amount when the surface of the unit adsorbent is covered with a single molecular layer of adsorbent, namely, the saturated adsorption amount, k_L (L mg^{-1}) is the Langmuir adsorption constant, and k_F and n are Freundlich adsorption constants.

The thermodynamic properties of CBCx adsorption on TC and ENR were further investigated by calculating the adsorption Gibbs free energy change (ΔG) [40] (equation (8)), the change in branding (ΔH), and the change in allosteric (ΔS) (equation (9)), which were used to study the spontaneous and thermal changes in the adsorption reactions.

$$\Delta G = -RT\ln K_c, \tag{8}$$

where R (8.314 J mol^{-1} k^{-1}) is the ideal gas constant and T (K) is the temperature.

In addition, ΔH and ΔS can be obtained according to the Van't Hoff equation [41]:

$$\ln \quad K_c = \frac{\Delta S}{R} - \frac{\Delta H}{RT}, \tag{9}$$

where K_c (equation (10)) is the adsorption allocation coefficient, which can be calculated as follows:

$$K_c = \frac{q_e}{C_e}. \tag{10}$$

3 Results and discussion

3.1 Characterization of CBC

Figure 2 shows the SEM analysis of untreated DB (a) and different CBCs. Figure 2(e) and (f) shows a compact shape with many small particles stacked together, which may be attributed to the over-addition of DB, resulting in the incomplete release of volatile components from the biomass and pore-clogging, thus showing a compact stacking pattern. Figure 2(b)–(d) show that the algal biochar has similar micro-morphology, and they all show well-

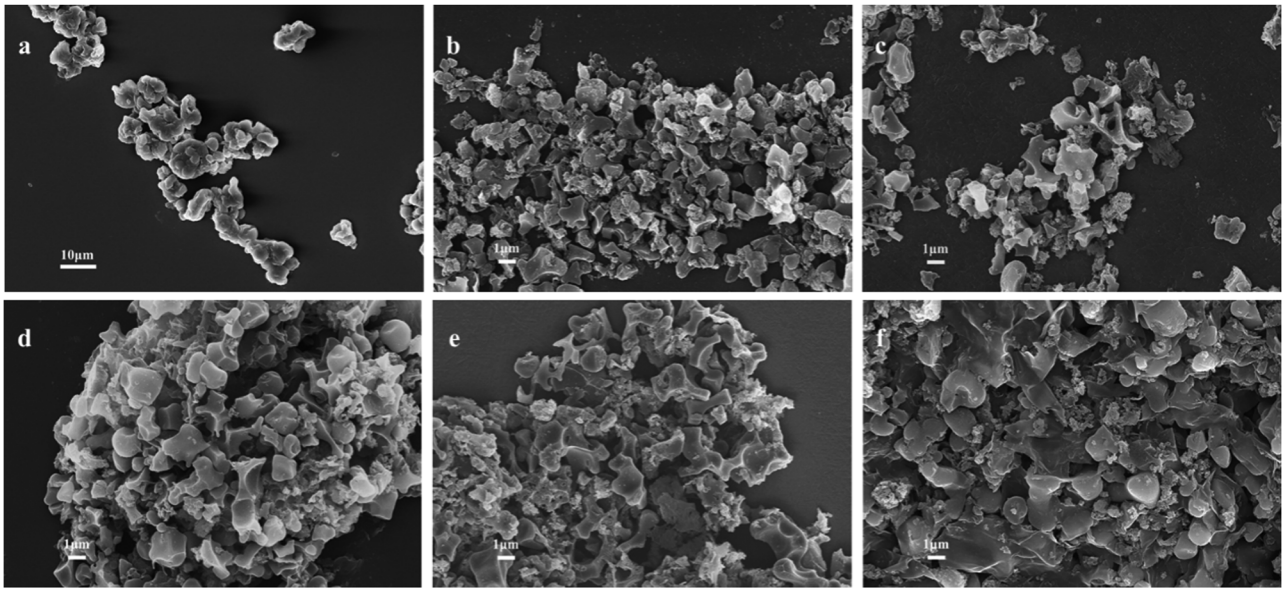

Figure 2: SEM images of DB(a), CBC 3(b), CBC 5(c), CBC 7(d), CBC 9(e), and CBC 11(f).

dispersed granularity and rough surface irregular shapes under the etching effect of KOH.

The changes in the specific surface area and pore structure of CBCs were investigated by adsorption and desorption of N_2, and the results are shown in Table 3. CBC 7 has the largest specific surface area value and the smallest average pore size. In our previous study, we found that the larger the specific surface area, the stronger the corresponding adsorption capacity, so we chose CBC 7 as the subsequent experimental object.

According to the X-ray diffractogram (Figure 3), it was found that the activated charcoal had a broad and slow diffuse diffraction peak at 2θ of 16–34° and 44° for (002) and (101) peaks of crystalline carbon fibers. This peak was found at 2θ of 16–34° for all the samples after charring, indicating that the microalgal biomass changed from organic compounds to finer-grained graphitized structure of amorphous carbon after charring. A stronger diffraction peak appeared at 2θ of 44°, where the height of CBC 7 was significantly lower than that of the other samples, suggesting that overfilling or underfilling with DB increases the crystallinity of the AC.

Table 3: BET surface areas, N_2 sorption capacity, and the average pore diameter of CBCs

Materials	BET specific surface area ($m^2\ g^{-1}$)	Average aperture (nm)
CBC 3	1483.298	3.324
CBC 5	1648.318	3.157
CBC 7	1971.843	3.156
CBC 9	1372.551	3.380
CBC 11	1216.443	3.941

3.2 Adsorption properties of CBC

CBC 7 was selected for the subsequent absorption experiments because it has the largest specific surface area value and the smallest average pore size. Orthogonal analysis

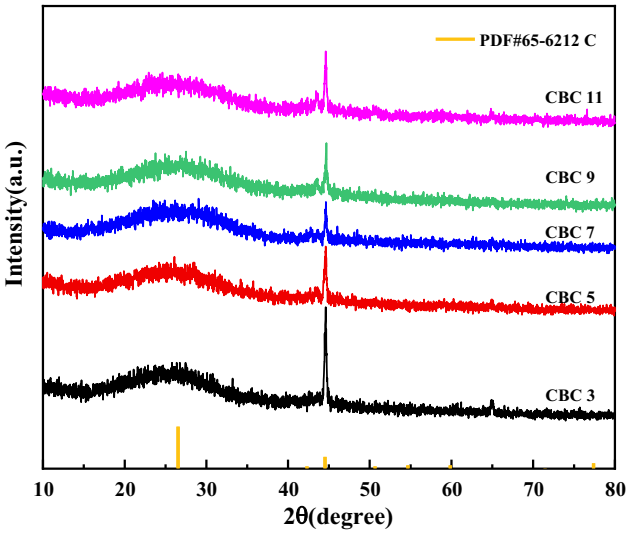

Figure 3: XRD spectra of CBC 3 (a), CBC 5 (b), CBC 7 (c), CBC 9 (d), and CBC 11 (e).

Table 4: ANOVA analysis of the removal rate (*R*)

Factor	DF	SS	MS	*F*	*P*
TC					
MCBC (g mL^{-1})	3	1.146	0.382	75.440	0.000
pH	2	0.101	0.051	10.007	0.001
MCBC (g mL^{-1}) × pH	6	0.135	0.022	4.428	0.004
Standard error	24	0.122	0.008		
Total	35	1.503			
ENR					
MCBC (g mL^{-1})	3	1.885	0.628	144.557	0.000
pH	2	0.068	0.034	7.871	0.002
MCBC (g mL^{-1}) × pH	6	0.043	0.007	1.649	0.177
Standard error	24	0.104	0.004		
Total	35	2.101			

was used to determine the optimal adsorption conditions of CBC 7 on TC and ENR.

The L16 orthogonal array orthogonal table was used to determine whether the adsorbent input and solution pH had a significant effect on the adsorption effect, and the structure is shown in Table 4.

From the ANOVA results, it can be observed that for TC, both adsorbent inputs showed significance (F = 75.440, p = 0.000 < 0.1), indicating the presence of a main effect and solution pH (F = 10.007, p = 0.001 < 0.1), suggesting that a main effect was present. For ENR, the adsorbent inputs all showed significance (F = 144.557, p = 0.000 < 0.1), indicating the presence of main effect and solution pH (F = 7.871, p = 0.002 < 0.1), indicating the presence of main effect.

As shown in Table 4, a comparison of TC and ENR was found to be a variance chi-square with P > 0.05 in the test of variance chi-square. From this, it was determined that the data fluctuations of multiple repetitions of orthogonal analysis experiments were consistent.

3.2.1 Effect of adsorbent dosage

As shown in Figure 4, increasing the dosage of CBC 7 adsorbent increased the removal rate. Under different pH conditions, the removal of TC and ENR reached 96 and 100%, respectively, when the dosage of CBC 7 was 0.004 g L^{-1}.

3.2.2 Effect of pH

As shown in Figure 4, when the dosage is certain, the removal of TC by CBC 7 reaches its maximum at pH 3, while the best pH for ENR is 7. This is because the structure of TC is very sensitive to pH. As shown in Figure 5, at pH 2–6, TC undergoes differential isomerization and the C4 conformation of the chiral carbon atom in the A-ring is changed, resulting in the formation of 4-epitetracycline hydrochloride [42]. After differential isomerization, the negative value of its specific spin is larger, which increases its solubility in water, resulting in a stronger adsorption capacity and higher removal rate by CBC.

Considering the effect of pH on the adsorption process, we determined the zeta potential and zero-charge point of the CBC 7 material. Figure 6a shows that the zeta potential of CBC 7 is −80 mV at pH 7, which indicates that CBC 7 is

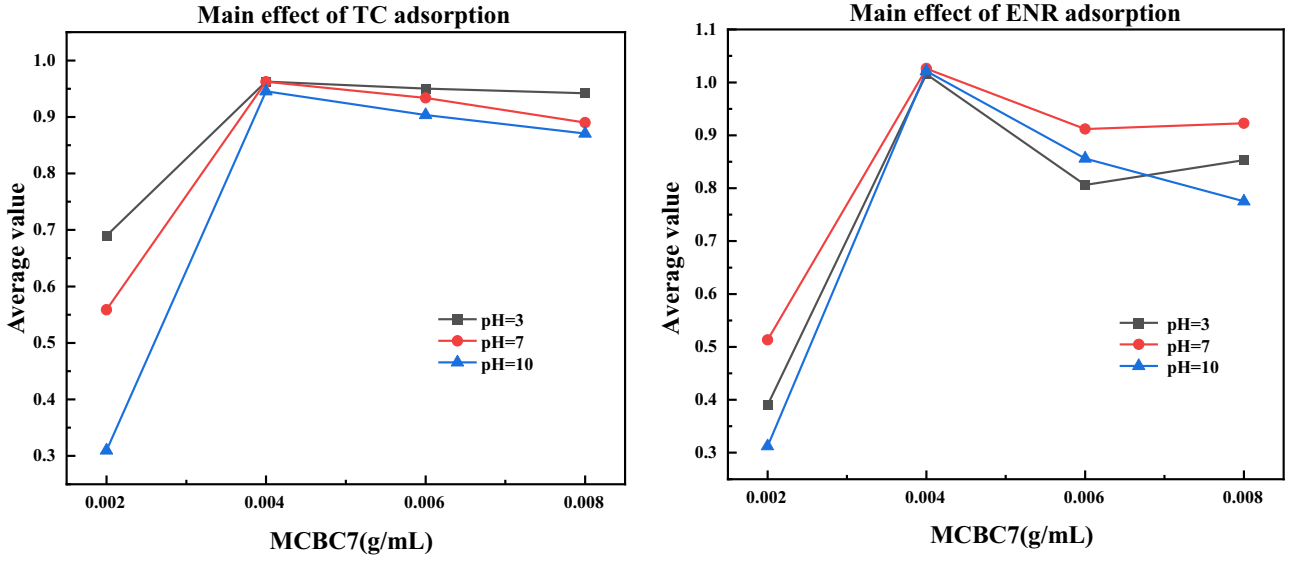

Figure 4: Comparison of two factors affecting the removal of TC and ENR.

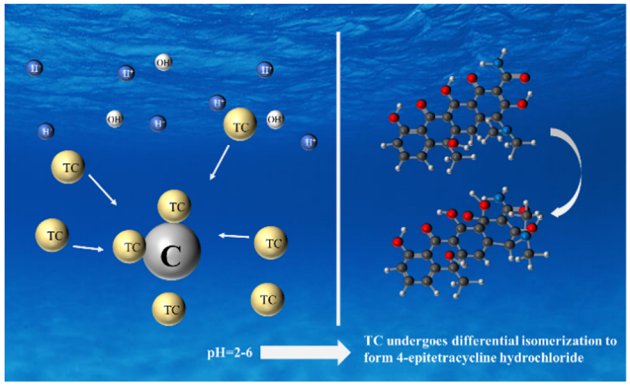

Figure 5: Structural comparison of tetracycline (left) and oxytetracycline (right).

highly electronegative and can be stably dispersed in aqueous solution [43].

Figure 6b shows that the point of zero charge (pH_{PZC}) of CBC 7 is 6.90. Zhou et al. [44] mentioned that when the solution pH < pH_{PZC}, the adsorbent is positively charged and tends to adsorb anions, and when pH > pH_{PZC}, the adsorbent is negatively charged and tends to adsorb cations. TC molecules form anions when they dissolve in water, so the adsorption rate of CBC 7 is the highest at pH < 6.90, i.e., at pH 3. For ENR, since the aqueous solution of ENR is cationic, the adsorption rate is highest at pH > 6.90, i.e., at pH 7.

3.3 Adsorption kinetics and thermostatic adsorption

The effect of adsorption time on the adsorption of TC and ENR by CBC 7 was studied by using pseudo-first-order, pseudo-second-order, and Elovich models. The results are shown in Figure 7 and Table 5.

Comparing the R^2 values of different kinetic models, it was found that the adsorption of both TC and ENR by CBC 7 was more consistent with the quasi-secondary kinetic model, which indicated that the main adsorption process between biochar and ENR and TC was subject to chemisorption. The equilibrium value of TC adsorption by CBC 7 was reached at 30 min, and the equilibrium value of ENR adsorption by CBC 7 was reached at 60 min.

Before reaching the adsorption equilibrium, TC and ENR molecules diffused to the surface of CBC 7, reacted with the adsorption sites, and adsorbed rapidly via electrostatic attraction and π–π bonding. Meanwhile, according to the SEM and BET results, the CBC has a large specific surface area and a small pore size, indicating that pore filling may also be one of the main adsorption mechanisms. With the increase of adsorption time, the adsorption sites on the surface of CBC 7 decreased and the pores were gradually filled intact to reach the adsorption equilibrium state.

Three temperature gradients of 298, 308, and 318 K were set in the isothermal adsorption experiment. Langmuir and Freundlich isotherm models were used to fit the adsorption equilibrium data, and the adsorption mechanism of ENR and TC adsorbed by CBC 7 was studied. The fitting results are shown in Figure 8, and the parameters are listed in Table 6.

The results of the adsorption isotherm analysis show that the Langmuir isotherm model could better indicate the process of ENR and TC adsorption by CBC 7. The highest correlation coefficient R^2 for TC adsorption by CBC 7 was 0.9797 at 318 K and the highest correlation coefficient R^2 for ENR adsorption by CBC 7 was 0.9988 at 298 K. This indicates

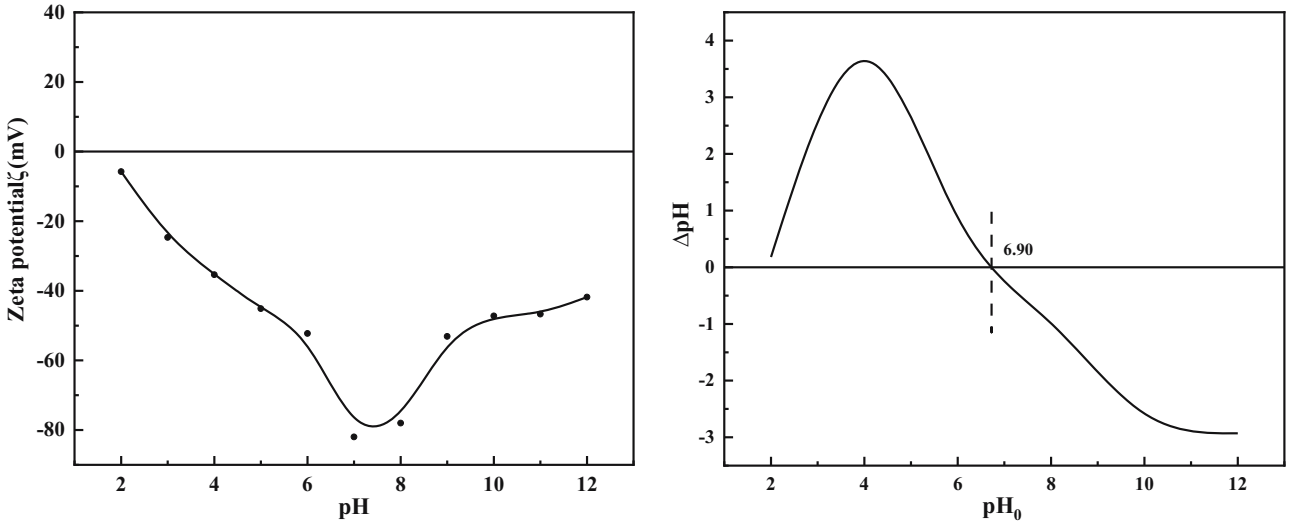

Figure 6: Zeta potential diagram and zero charge point diagram of CBC 7.

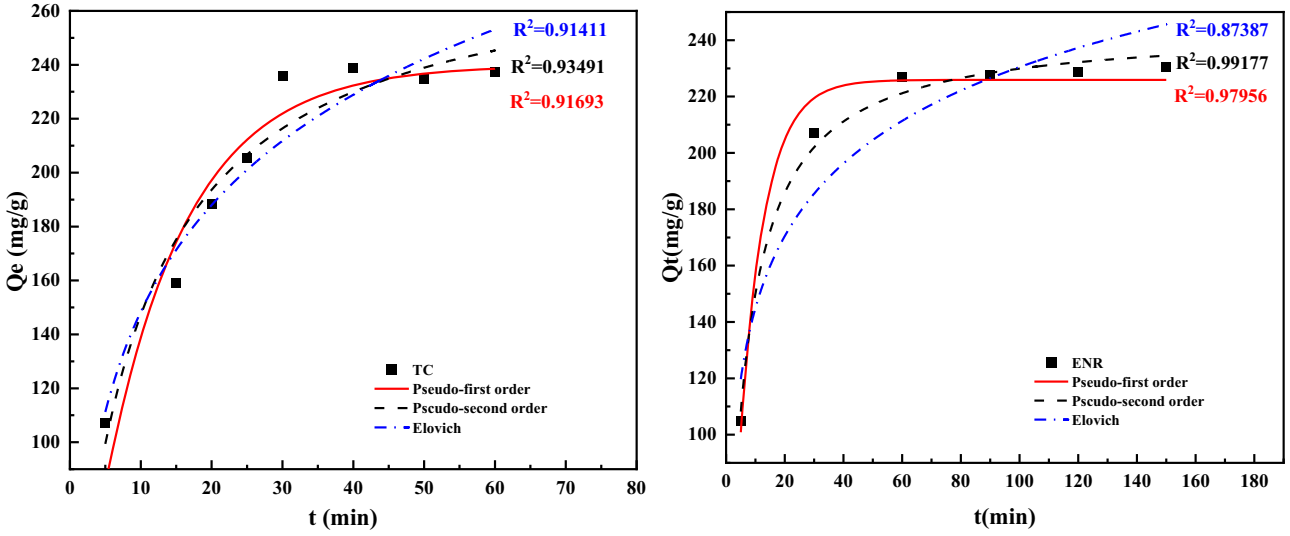

Figure 7: Fitting curves of different kinetic models for the adsorption of TC and ENR on CB7.

that CBC 7 adsorbs both TC and ENR as monolayer. Also, calculated according to the Langmuir model, the q_m value represents the maximum adsorption of CBC. The maximum adsorption values of CBC on TC and ENR were found to be 299.8974 and 352.6736 mg g^{-1}.

Table 5: Variance chi-square tests

F	df1	df2	P
TC			
2.022	11	24	0.072
ENR			
0.878	11	24	0.573

3.4 Adsorption thermodynamics

In order to study the thermodynamic properties of TC and ENR adsorbed by CBC 7, the isotherms of TC and ENR adsorbed by CBC 7 were investigated at 298, 308, and 318 K, respectively (as shown in Figure 8). By calculating the Gibbs free energy change (Δ*G*), enthalpy change (Δ*H*), and entropy change (Δ*S*) of TC and ENR adsorbed by CBC 7,

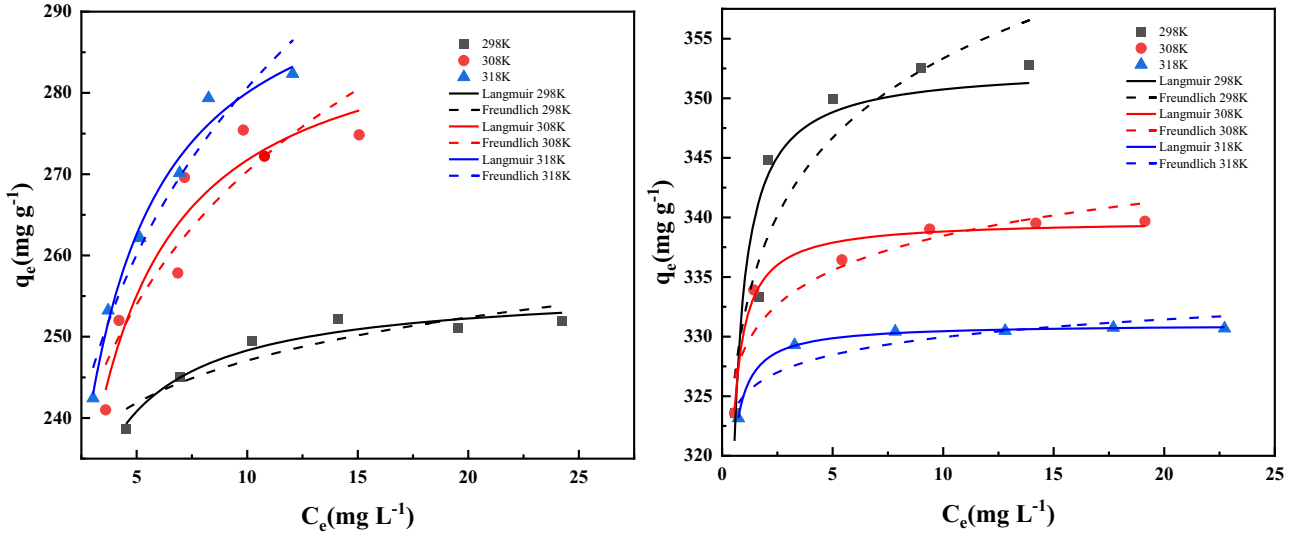

Figure 8: According to different isothermal models, the adsorption equilibrium diagrams of TC and ENR adsorbed by CB7 at 298, 308, and 318 K are fitted.

Table 6: Fitting parameters of different adsorption kinetic models

Type of dynamic equation	Model parameter	TC	ENR
Pseudo-first-order	Q_e (mg g^{-1})	223.9164	225.9209
	k_1 (min^{-1})	0.9173	0.8884
	R^2	0.9169	0.97956
Pseudo-second-order	Q_e (mg g^{-1})	283.0728	244.3649
	K_2 [g (mg min)$^{-1}$]	0.0003	0.0006
	R^2	0.93491	0.9917
Elovich	α [g (mg min^{-1})$^{-1}$]	1.03504	4.6815
	β [g mg^{-1}]	0.0163	0.0266
	R^2	0.91411	0.87387

the spontaneous and thermal changes of adsorption reactions are further explored, and the results are shown in Tables 7 and 8.

The negative values of ΔG for the CBC 7 adsorbed TC and ENR systems at all three temperatures indicate the interaction and spontaneous proceeding of the CBC 7 adsorbed TC and ENR [45]. The negative value of ΔS is due to the migration of TC and ENR molecules from the liquid phase to the adsorbed state, resulting in the loss of degrees of freedom and the decrease of entropy value. The negative value of ΔH further confirms that the adsorption of TC and ENR by CBC 7 is an exothermic process.

3.5 Analysis of adsorption of TC and ENR mechanism.

3.5.1 FT-IR analysis of CBC 7 before and after adsorption

The changes in surface functional groups before and after the adsorption of TC and ENR by CBC 7 were analyzed by FT-IR. As shown in Figure 9, the broad peak at 3,740–3,008 cm^{-1} is the –OH stretching vibration peak with obvious vibration amplitude and in-plane bending vibration. CBC 7 + TC and CBC 7 + ENR are compared with CBC 7, and it can be found

Table 8: Thermodynamic parameters of adsorption of TC and ENR by CBC 7

	T (K)	ΔG (kJ mol^{-1})	ΔS (J mol^{-1})	ΔH (kJ mol^{-1})
TC	298	−0.2625	−1.1421	−0.0443
	308	−0.0798		
	318	−0.0765		
ENR	298	−14.2411	−0.3805	−1.84388
	308	−14.3231		
	318	−14.6405		

that the absorption peak is blue-shifted after adsorption, which indicates that –OH is involved in the adsorption of TC and ENR by CBC 7. 2,925 cm^{-1} or so is the C–H stretching vibration peak in –CH2. The C═O stretching vibration peak in the aromatic ring appeared at around 1,589 cm^{-1}, which decreases in intensity after the adsorption of TC. The peak at 1,458 cm^{-1} is the C═C stretching vibration peak, which indicates that the surface of CBC contains a stable aromatic

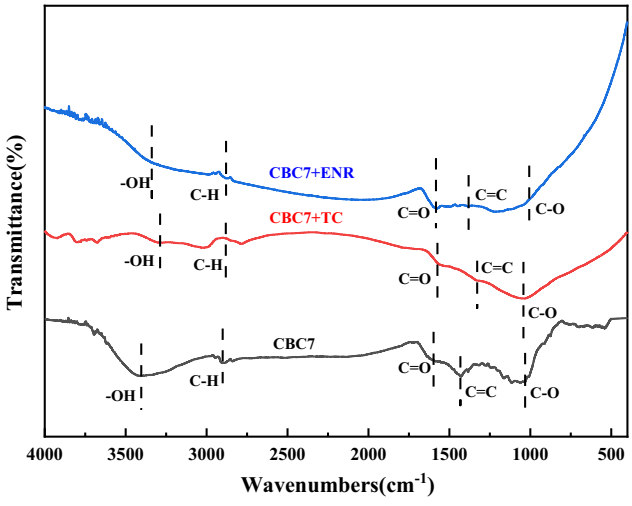

Figure 9: FT-IR spectra of CBC 7, CBC 7 + ENR, and CBC 7 + TC after adsorption.

Table 7: Fitting parameters of the isothermal adsorption model at different temperatures

Antibiotic	T (K)	Langmuir model			Freundlich model		
		K_L (L mg^{-1})	Q_m (mg g^{-1})	R^2	K_F [mg g^{-1}(mg L^{-1})$^{-1/n}$]	n	R^2
TC	**298**	3.1083	256.2995	0.9455	217.9961	9.1157	0.9416
	308	1.4301	290.7355	0.8737	219.6609	11.0889	0.7889
	318	1.4086	299.8974	0.9797	230.1662	32.5097	0.7967
ENR	**298**	18.1316	352.6736	0.8554	331.6835	36.4033	0.8507
	308	35.7791	339.7691	0.9780	328.8956	80.3212	0.8377
	318	55.4029	331.0529	0.9988	325.0539	153.8462	0.8078

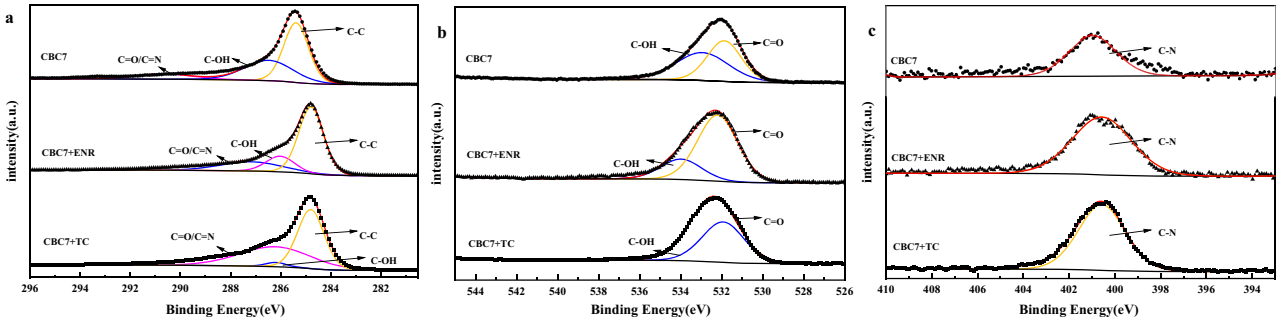

Figure 10: XPS analysis of CBC 7, CBC 7 + ENR, and CBC 7 + TC: C (a), O (b), and N (c).

skeleton, and the intensity of the adsorption peaks of CBC 7 + TC and CBC 7 + ENR are reduced compared with that of CBC 7. The peak at 1,041 cm^{-1} is the absorption peak of C–O. The absorption peak of the bond stretching vibration at 1,041 cm^{-1} indicates that the surface of the material contains lipid compounds.

3.5.2 XPS analysis of CBC 7

Figure 10 shows the XPS energy spectrum analysis of CBC 7 before and after adsorption of TC and ENR. Figure 10(a) shows the C1s spectrum. Before adsorption, the C–C peak appears at 284.84 eV, C–OH at 286.05 eV, and C═O at 289.78 eV. This is a vibrational peak due to π═π bond in the aromatic ring [46]. The C–C, C–OH, and C═O binding energies showed some degree of displacement and change after the adsorption of TC and ENR, indicating that hydroxyl and carbonyl groups were involved in the reaction during the adsorption process [47–49]. Figure 10(b) shows the O1s spectrum with the change of C═O peak intensity before and after adsorption, and the C–OH bond binding energy was significantly decreased after adsorption of TC, indicating the involvement of hydroxyl-containing functional groups in the adsorption process [50], which is consistent with the results of IR spectral analysis.

4 Conclusion

In this study, a low-cost adsorbent CBC was prepared from DB for the removal of TC and ENR by comparing different DB input amounts by SEM, XRD, and BET. It was found that the prepared CBC 7 had the largest specific surface area with the optimal adsorption effect when the DB input amount was 7. Using orthogonal experiments, the removal rate of 100 mg L^{-1} TC by adsorption of 0.004 g of CBC 7 for 30 min at pH 3 was determined to be 96%. The removal rate of 100 mg L^{-1} ENR by 0.004 g of CBC 7 adsorption for 60 min at pH 7 was 100%. The adsorption process of TC and ENR by CBC followed the Langmuir model and the pseudo-secondary kinetic model, indicating that the adsorption rate was influenced by chemisorption. CBC 7 was effective in removing the relevant pollutants in the aqueous environment. Similarly, microalgae feedstock has a significant bio-oil yield compared to other feedstock biomass, which can be used as an energy source for sustainable and green production processes. In turn, this study demonstrated the excellent pollutant removal performance of algal biochar, highlighting the great potential of microalgae-based biochar for application.

Funding information: This work was financially supported by the Natural Science Foundation of Jiangxi Province (Grant 20232BAB205005).

Author contributions: Wang Feiyan: data curation and original draft. Zhang Yali: review and editing. Luo Siling: investigation. Chen Zhiqin: methodology. Luo Shanshan: visualization. Wenkui Li: conceptualization, review, and editing.

Conflict of interest: The authors state no conflict of interest.

Ethical approval: The conducted research is not related to either human or animal use.

Data availability statement: The datasets generated during and/or analyzed during the current study are available from the corresponding author on reasonable request.

References

[1] Tayyab M, Kulsoom UE, Liu Y, Mansoor S, Khan M, Akmal Z, et al. Visible light-driven photocatalytic H_2 evolution and dye

degradation by electrostatic self-assembly of CdS nanowires on Nb_2C MXene. Int J Hydrog Energy. 2024;51:1400–13.
[2] Tayyab M, Liu Y, Xu Z, Aman S, Yue W, Irfan RM, et al. Integration of redox cocatalysts for photocatalytic hydrogen evolution. UV-Visible Photocatalysis for Clean Energy Production and Pollution Remediation: Materials, Reaction Mechanisms, and Applications. Wiley; 2023. p. 93–107.
[3] Bashir M, Batool M, Arif N, Tayyab M, Zeng YJ, Zafar MN. Strontium-based nanomaterials for the removal of organic/inorganic contaminants from water: A review. Coord Chem Rev. 2023;492:215286.
[4] Cheng N, Wang B, Wu P, Lee X, Xing Y, Chen M, et al. Adsorption of emerging contaminants from water and wastewater by modified biochar: A review. Environ Pollut. 2021;273:116448.
[5] Liu B, Zhang SG, Chang CC. Emerging pollutants-Part II: Treatment. Water Environ Res. 2019;91(10):1390–401.
[6] Tayyab M, Liu Y, Min S, Irfan RM, Zhu Q, Zhou L, et al. Simultaneous hydrogen production with the selective oxidation of benzyl alcohol to benzaldehyde by a noble-metal-free photocatalyst VC/CdS nanowires. Chin J Catal. 2022;43(4):1165–75.
[7] Tayyab M, Liu Y, Liu Z, Pan L, Xu Z, Yue W, et al. One-pot in-situ hydrothermal synthesis of ternary In2S3/Nb2O5/Nb2C Schottky/S-scheme integrated heterojunction for efficient photocatalytic hydrogen production. J Colloid Interface Sci. 2022;628:500–12.
[8] Bound JP, Voulvoulis N. Household disposal of pharmaceuticals as a pathway for aquatic contamination in the United Kingdom. Environ Health Perspect. 2005;113(12):1705–11.
[9] Asante-Sackey D, Rathilal S, Tetteh EK, Armah EK. Membrane bioreactors for produced water treatment: A mini-review. Membranes. 2022;12(3):275.
[10] Judd S. The status of membrane bioreactor technology. Trends Biotechnol. 2008;26(2):109–16.
[11] Dhangar K, Kumar M. Tricks and tracks in removal of emerging contaminants from the wastewater through hybrid treatment systems: A review. Sci Total Environ. 2020;738:140320.
[12] Mirzaei A, Chen Z, Haghighat F, Yerushalmi L. Removal of pharmaceuticals and endocrine disrupting compounds from water by zinc oxide-based photocatalytic degradation: A review. Sustain Cities Soc. 2016;27:407–18.
[13] Hussain SM, Hussain T, Faryad M, Ali Q, Ali S, Rizwan M, et al. Emerging aspects of photo-catalysts (TiO_2 & ZnO) doped zeolites and advanced oxidation processes for degradation of azo dyes: A review. Curr Anal Chem. 2021;17(1):82–97.
[14] Zhang W, Qiao X, Chen J. Preparation and photocatalytic activity of photocatalytic nanomaterials. Chemistry. 2005;68(11):839–44,838.
[15] Motitswe MG, Badmus KO, Khotseng L. Development of adsorptive materials for selective removal of toxic metals in wastewater: A review. Catalysts. 2022;12(9):1057.
[16] Zhao L, Sun ZF, Pan XW, Tan JY, Yang SS, Wu JT, et al. Sewage sludge derived biochar for environmental improvement: Advances, challenges, and solutions. Water Res X. 2023;18:100167.
[17] Feng Y, Cui Q, Xie Y, Zhao M, Zhang J, Dong X. Research progress on modification of magnetic chitosan microspheres and its application in water treatment. Acta Materiae Compositae Sin. 2022;39(6):2543–55.
[18] Ye YF, Qu Y, Sun JM. Functionalized mesoporous SiO_2 materials for CO_2 capture and catalytic conversion to cyclic carbonates. Catal Reviews-Sci Eng. 2023;1–56.
[19] Grela A, Kuc J, Bajda T. A review on the application of zeolites and mesoporous silica materials in the removal of non-steroidal anti-inflammatory drugs and antibiotics from water. Materials. 2021;14(17):4994.
[20] Menshova II, Zabolotnaya E, Chelnokov VV, Garabadzhiu AV. Adsorption of organic substances using zeolites. Izvestiya Vysshikh Uchebnykh Zavedenii Khimiya I Khimicheskaya Tekhnologiya. 2021;64(8):131–8.
[21] Palliyarayil A, Saini H, Vinayakumar K, Selvarajan P, Vinu A, Kumar NS, et al. Advances in porous material research towards the management of air pollution. Emergent Mater. 2021;4(3):607–43.
[22] Olajire AA. Synthesis of bare and functionalized porous adsorbent materials for CO2 capture. Greenh Gases: Sci Technol. 2017;7:399–459.
[23] Kamarudin NS, Dahalan FA, Hasan M, An OS, Parmin NA, Ibrahim N, et al. Biochar: A review of its history, characteristics, factors that influence its yield, methods of production, application in wastewater treatment and recent development. Biointerface Res Appl Chem. 2022;12(6):7914–26.
[24] Kumar A, Singh E, Mishra R, Lo SL, Kumar S. A green approach towards sorption of CO_2 on waste derived biochar. Environ Res. 2022;214:113954.
[25] Sinha R, Kumar R, Sharma P, Kant N, Shang JY, Aminabhavi TM. Removal of hexavalent chromium via biochar-based adsorbents: State-of-the-art, challenges, and future perspectives. J Environ Manag. 2022;317:115356.
[26] Kurniawan TA, Othman MHD, Liang X, Goh HH, Gikas P, Chong K-K, et al. Challenges and opportunities for biochar to promote circular economy and carbon neutrality. J Environ Manag. 2023;332:117429.
[27] Zhou H, Wang Z, Gao C, Sun Q, Liu J, She D. Synthesis of honeycomb lignin-based biochar and its high-efficiency adsorption of norfloxacin. Bioresour Technol. 2023;369:128402.
[28] Torri C, Samorì C, Adamiano A, Fabbri D, Faraloni C, Torzillo G. Preliminary investigation on the production of fuels and bio-char from Chlamydomonas reinhardtii biomass residue after bio-hydrogen production. Bioresour Technol. 2011;102(18):8707–13.
[29] Tso CY, Chao CYH. Activated carbon, silica-gel and calcium chloride composite adsorbents for energy efficient solar adsorption cooling and dehumidification systems. Int J Refrig-Revue Internationale Du Froid. 2012;35(6):1626–38.
[30] Wang X, Liu Y, Li W, Gong Y, Wang C, Shi Z. Effects and mechanisms of methyl orange adsorption from aqueous solutions by algal biochar. Technol Water Treat. 2021;47(7):42–47,53.
[31] Chen YD, Lin YC, Ho SH, Zhou Y, Ren NQ. Highly efficient adsorption of dyes by biochar derived from pigments-extracted macroalgae pyrolyzed at different temperature. Bioresour Technol. 2018;259:104–10.
[32] Siddiki SYA, Mofijur M, Kumar PS, Ahmed SF, Inayat A, Kusumo F, et al. Microalgae biomass as a sustainable source for biofuel, biochemical and biobased value-added products: An integrated biorefinery concept. Fuel. 2022;307:121782.
[33] Rashid N, Rehman MSU, Han J-I. Recycling and reuse of spent microalgal biomass for sustainable biofuels. Biochem Eng J. 2013;75:101–7.
[34] Nguyen TB, Nguyen V, Hoang HG, Cao NDT, Nguyen TT, Vo TDH, et al. Recent development of algal biochar for contaminant remediation and energy application: a state-of-the art review. Curr Pollut Rep. 2023;9(1):73–89.
[35] Folch J, Lees M, Sloane Stanley GH. A simple method for the isolation and purification of total lipides from animal tissues. J Biol Chem. 1957;226:497–509.

[36] Eris S, Bashiri H. Kinetic study of the adsorption of dyes onto activated carbon. Prog React Kinetics Mechanism. 2016;41(2):109–19.
[37] Rassaei F. Adsorption kinetics and isotherm modeling of lead in calcareous soils: Insights into thermodynamics, desorption, and soil properties. Commun Soil Sci Plant Anal. 2023;54(15):2059–76.
[38] Li JQ, Xie XY, Zhang QH, Xing ZY. Reliable measurements of low-density plasmas using a novel Langmuir probe with a guard tube. Plasma Phys Controlled Fusion. 2023;65(3):035009.
[39] Debord J, Chu KH, Harel M, Salvestrini S, Bollinger JC. Yesterday, Today, and Tomorrow. Evolution of a Sleeping Beauty: The Freundlich Isotherm. Langmuir. 2023;39(8):3062–71.
[40] Zhou Q, Wen B, Zhang JL, Liu F, Ouyang XP, Liang YL, et al. Influence of graphite Gibbs surface free energy on the initial viscosity and stability of traditional anode slurry in lithium-ion batteries. J Cent South Univ. 2023;30(3):665–76.
[41] Motati R, Kandi T, Acree WE. Comments on “Solubility measurement, thermodynamic modeling and solubility parameters of clarithromycin (Form vertical bar vertical bar) in aqueous ethanolic solution”. Phys Chem Liq. 2023;61(3):226–8.
[42] Doerschuk AP, Bitler BA, McCormick JR. Reversible isomerizations in the tetracycline family. J Am Chem Soc. 1955;77(17):4687.
[43] Ho SH, Yang ZK, Nagarajan D, Chang JS, Ren NQ. High-efficiency removal of lead from wastewater by biochar derived from anaerobic digestion sludge. Bioresour Technol. 2017;246:142–9.
[44] Zhou Y, Lu J, Zhou Y, Liu Y. Recent advances for dyes removal using novel adsorbents: A review. Environ Pollut. 2019;252:352–65.
[45] Zhang SY, Jin WW, Wang D, Xu D, Zhang JRY, Shattuck MD, et al. Local and global measures of the shear moduli of jammed disk packings. Phys Rev E. 2023;107(5):054903.
[46] Tien HW, Huang YL, Yang SY, Wang JY, Ma CCM. The production of graphene nanosheets decorated with silver nanoparticles for use in transparent, conductive films. Carbon. 2011;49(5):1550–60.
[47] Wang R, Lai X, Li J, Chang H, Zhang G. Adsorption of nitrate nitrogen by peanut shell biochar. J Agro-Environ Sci. 2016;35(9):1727–34.
[48] Fu Z, Chen YR, Lu YY, Wang Y, Chen JH, Zhao YX, et al. KMnO4 modified biochar derived from swine manure for tetracycline removal. Water Pract Technol. 2022;17(11):2422–34.
[49] Wang HX, Zhang ML, Lv Q. Removal efficiency and mechanism of Cr (VI) from aqueous solution by maize straw biochars derived at different pyrolysis temperatures. Water. 2019;11(4):781.
[50] Choudhary B, Paul D, Singh A, Gupta T. Removal of hexavalent chromium upon interaction with biochar under acidic conditions: mechanistic insights and application. Environ Sci Pollut Res. 2017;24(20):16786–97.